Lawrence Berkeley National Laboratory

Title
Manipulating the Crystallization Kinetics by Additive Engineering toward High-Efficient Photovoltaic Performance

Permalink
https://escholarship.org/uc/item/32r2g50w

Authors
Song, Jingnan
Hu, Qin
Zhang, Quanzeng
et al.

Peer reviewed

Manipulating the crystallization kinetics by additive engineering toward high-efficient photovoltaic performance

Jingnan Song,[a] Qin Hu,[bc] Shaobing Xiong,[d] Quanzeng Zhang,[a] Zhe Zhao,[a] Jazib Ali,[a] Yecheng Zou,[e] Wei Feng,[e] Zhibin Yang,[a] Qinye Bao,[d] Yongming Zhang,[a] Thomas P. Russell,[bc] Feng Liu*[a]

[a]Frontiers Science Center for Transformative Molecules and In-situ Center for Physical Science, School of Chemistry and Chemical Engineering, Shanghai Jiao Tong University, Shanghai 200240, China

[b]Department of Polymer Science and Engineering, University of Massachusetts, Amherst, MA 01003, USA

[c]Advanced Light Sources, Lawrence Berkeley National Laboratory, CA 94720, USA

[d]Key Laboratory of Polar Materials and Devices, Ministry of Education, East China Normal University, 200241 Shanghai, PR China

[e]State Key Laboratory of Fluorinated Functional Membrane Materials, Zibo City, Shandong 256401, China

*Address correspondence to: fengliu82@sjtu.edu.cn

ABSTRACT

Additive engineering has been proven to be an effective method to improve the efficiency and stability of perovskite solar cells, but its intrinsic role in directing the crystallization pathway remains unknown. Here, *in situ* grazing-incidence wide-angle x-ray scattering (GIWAXS) is applied to study the function of 1,8-diiodooctane (DIO) additive in manipulating the crystallization behavior of perovskite. The results show

that a proper amount of DIO additive induces multi-stage intermediate crystallization phases and increases the activation energy for nucleation and growth, which postpones the perovskite phase transformation time and broadens the transition zone. The elongated crystallization process affords a desired perovskite film with improved crystallinity and reduced defect density, further enabling a longer carrier diffusion length. As a result, a higher device efficiency of 20.39% is achieved, and improved moisture and thermal stability are recorded. This study provides a new understanding on the role of solvent additive that could guide the proper selection of processing conditions to manipulate the perovskite crystallization pathways toward high device performance.

Keywords: *In situ* characterization, crystallization kinetics, activation energy, DIO additive, perovskite solar cells

Broader context

Over the past years, great achievements have been made in improving the device efficiency of perovskite solar cells that now is over 25%. The perovskite layer fabrication, in which processing conditions play an important role in controlling thin film morphology, strongly influences the device performances. Behind the varied conditions, the underlying crystallization kinetics should be concerned since it is the major factor that dictates thin film morphology. In this report, we use *in situ* grazing-incidence wide-angle x-ray scattering (GIWAXS) and crystallization growth analysis to show the role of DIO additive in perovskite crystallization. We see that DIO strongly influences the intermediate phase transition towards perovskite crystallization, and its amount acts as an important phase regulator to control the crystallization kinetics and crystallinity. Thus such additive processing provides a new handle that can be utilized to manipulate thin film morphology, and an improved device efficiency of 20.39% is obtained, which is ~12% higher than control device without morphology optimization.

Introduction

Organic-inorganic hybrid perovskite solar cells have experienced an unprecedented rise in device efficiency from 3.8% in 2009 up to the current certified power conversion efficiency of 25.2%,[1, 2] close to efficiency record of silicon solar cells. Additive processing plays a critical role in this efficiency improvement. Additives of different kinds, and of different functions, including organic halide salts (e.g. methylamine chloride (MACl), guanidinium bromide (GABr)),[3-5] metal halide salts (e.g. cesium iodide (CsI), rubidium iodide (RbI), potassium iodide (KI), and sodium fluoride (NaF)),[6-11] polymers (e.g. poly(4-vinylpyridine) (PVP), poly(methyl methacrylate) (PMMA), and polyethylene glycol (PEG)),[12-15] and small molecules (e.g., pyridine, thiophene, and fullerenes),[16-18] have been used to improve the quality of perovskite films with excellent morphology and crystallinity. Besides the solid additives, the solvent additives with high-boiling points, such as dimethyl sulfoxide (DMSO), N-methyl-2-pyrrolidone (NMP), and 1,8-iodooctane (DIO), were also introduced into the perovskite precursors to improve the film quality and device performance.[19-24]

Although the success of additive processing has been achieved in improving device performance, the underlying mechanism in morphology manipulation during perovskite film formation is not clear. The deficiency in such study is due partially to the complicated multicomponent perovskite precursor crystallization, and partially to the difficulties in characterization. Recently, *in situ* grazing-incidence wide-angle x-ray scattering (GIWAXS) has emerged as a powerful technique to study the crystallization behavior and formation mechanism of perovskite films from the intermediate adduct or the precursor solution to the final solid state.[25-29] Previously, we have shown that the crystallization of classic $MAPbI_3$ perovskite thin film underwent through an important intermediate phase transition process to form the cubic perovskite lattices.[27] And more recently, we show the details of two-dimensional (2D) perovskite crystallization, during which intermediate phase transition is affected by the alkali metal ions and

solvent molecules additives.[28] Besides, the functions of halide and cation ions in regulating the crystallization process have also been unraveled by *in situ* GIWAXS in the case of mixed perovskite films.[30-33] For example, Amassian and coworkers found that the halide and cation engineering could widen the anti-solvent processing window for easy fabrication of high-quality perovskite films.[31] And Lu's group reported that Cs^+ could manipulate the crystallization pathway to avoid the formation of secondary phases.[32]

Comparing to the above-mentioned progress, solvent additives, which present only shortly during film formation, and vaporizes in dried perovskite thin films, is of high interest in understanding detailed intermediate phase transition in perovskite thin films. In this study, we use 1,8-diiodooctane (DIO) as the model system to investigate its impact on perovskite crystallization. We see that DIO molecules interact with intermediate adduct via a multi-stage mechanism to regulate the crystallization process. The strong cooperation enables high activation energy E_a, which slows down the crystallization process and provides enough time for the crystallization and growth of perovskites, finally affording a high-qualified perovskite film. Such film exhibits improved crystallinity and reduced trap density, gave rise to reduced non-radiative recombination and prolonged carrier diffusion length. As a result, the champion device efficiency of 20.39% was achieved, and improved moisture and thermal stability was recorded, confirming the success of DIO additive processing.

Results and discussion

In situ GIWAXS measurements were conducted to monitor the crystallization evolution process from the precursor solution to the final perovskite film, from which the crystallization kinetics and the role of DIO in altering the phase formation pathways can be extracted. **Fig. S1** shows a series of 2D GIWAXS images at different drying stages. By circular integrating on each of the 2D GIWAXS images, the *in situ* 1D intensity-time profiles for slot-die printed perovskite films with different amount of DIO additives can be obtained, with results shown in **Fig. 1a, c, e,** and the

corresponding 2D color mappings as a function of q and frames are summarized in **Fig. S2**. Further, the intensity evolution of characteristic peaks and peak position of intermediate phase were analyzed by fitting the diffraction peaks using the Gauss mode, as shown in **Fig. 1b, d, f**. (Here, perovskite films prepared from X vol% DIO with respect to main solvent were abbreviated as DIOX). In all cases, two broad scattering halos were observed. One is located at low-q region, which is associated with inter-distances of the $[PbI_6]^{4-}$ cages in the precursor solution. Another is located at high q values (1.4~2.0 Å^{-1}), which is ascribed to the inter-distances of solvent molecules and atoms in perovskites. As the solvent evaporated, these two broad diffusive reflections gradually evolved toward higher q values, indicating the gradually decreased inter-distance between $[PbI_6]^{4-}$ cages, finally forming the orderly arranged intermediate phase. With time evolving, a phase transition process is observed, during which the peak intensity of the intermediate phase gradually decreased and the peak intensity of perovskite phase increased. For the DIO0 case, the phase transition occurred at around 470 s (Frame 105) shortly after the formation of stabilized intermediate phase (pink dashed line in **Fig 1b**). Except for the perovskite peak (q=1.0 Å^{-1}, violet dashed line in **Fig 1b** as the starting point), new sharp peaks occur at q<1.0 Å^{-1} quickly after the appearance of perovskite phase, which are attributed to the crystalline complex phase (q=0.437 Å^{-1}), MAI (q=0.667 Å^{-1}), yellow δ-phase (q=0.84 Å^{-1}), and PbI$_2$ phase (q=0.90 Å^{-1}), respectively. These byproducts formation is due to the crystallization instability of perovskite phase transformation, which leads to low quality perovskite thin films that deteriorate the device function under room temperature printing fabrication. When we add DIO additives into the perovskite precursor solution, a direct phase transition from the scattering halo to perovskite phase is observed with negligible by-products (**Fig. 1c-f**). For the DIO1 case (**Fig. 1c, d**), the peak position of intermediate phase scattering at low-q region first shifts to high-q value, and then reorganized slightly to low-q value, with key turning point marked by pink dashed lines in **Fig 1d**. The high q plateau (space marked by first two pink dashed lines) is slightly tighter comparing to DIO0 case, and thus the presence of

DIO thinning the shell of intermediate $[PbI_6]^{4-}$ cages, by replacing surrounding solvent molecules with DIO, and probably forms $MAI·PbI_2·DIO$ adducts. The slightly dropping in intermediate phase q position (space marked by the second and third pink dashed lines) is in concurrence of perovskite phase formation (violet dashed line in **Fig 1d** marks the starting point), indicating a specific $[PbI_6]^{4-}$ cage reorganization to get registered into perovskite lattices. The multi-stage intermediate phase process and the low volatile nature of DIO account for the postponed phase transition time point (600 s for DIO1 case). Moreover, the stronger interaction between $[PbI_6]^{4-}$ cage and DIO slows the crystallization process and induces a wider phase transition zone with less solvent interaction, thus a more flexible crystallization window is obtained, and perovskite precursors could get into cubic lattice more elegantly, to form a better crystalline morphology. We then add 5 vol% of DIO into precursor solution to investigate the up limit of the DIO controlled perovskite crystallization process. As expected, the crystallization profile changes largely. The intermediate phase and phase transition can still be seen, but in an uncontrolled manner. A sharp intensity growing of intermediate phase is recorded, which maximized at around 40 frames. And perovskite transformation is seen around frame 220. A large time window existed without detailed structure change, and such behavior is due to the slow vaporization of excessive DIO, which needs to be reduced to a low volume to induce $[PbI_6]^{4-}$ cage to perovskite phase transition. The intermediate phase peak position in associating with peak intensity tells the details of precursor solution changes. A quick change in peak position before first pink dashed line is due to DMF solvent vaporization, and the slower peak position change in-between first two dashed pink lines is due to DIO evaporation. When excess DIO is vaporized, the peak position shifts to slightly higher position, similar to that observed in the plateau region in DIO1 case. And perovskite formation takes place in DIO rich environment that leads to difficulties in forming into high quality large crystalline domain. And the thin film crystallinity in DIO5 case is much lower comparing to previous two samples, as indicated by a broad and intensive halo across 1.2-2.5 $Å^{-1}$ region, which summarizes the amorphous molecules and atoms

distances (**Fig. S3**). We further extended the study to DIO10 condition, which yields a similar crystallization process with results shown in **Fig. S4** and **S5**. The above results suggest that DIO plays a critical role in altering the film crystallization pathway, and a proper DIO amount must be used to ensure its intercalation into $[PbI_6]^{4-}$ cage in intermediate phase to control the perovskite phase transformation.

The crystallization mechanisms deduced from *in situ* GIWAXS results are illustrated in **Fig. 2**. In a starting solution, the PbI_2 and MAI were dissolved in DMF solvents. Solvent evaporation leads to the formation of intermediate phases due to the preferential interaction between PbI_2 and DMF molecules, which then transform into perovskite phases. In the control case, the weak coordination between Pb^{2+} and DMF molecules as well as the low boiling point of DMF results in a quick nucleation and fast phase transition process. The time is short that the perovskite phase transformation takes place in an uncontrolled manner to form multiple products that reduces thin film quality and low crystallinity. The introduction of DIO additive changes the crystallization kinetics by manipulating the phase transformation. A key transformation intermediate state, of replacing DMF with DIO, marked by the scattering peak position change, results in highly controllable crystallization pathway. The stronger interaction between Pb^{2+} and DIO slows down the phase transformation, which provides longer time window for perovskite crystallization, leading to large crystalline domain and better crystal quality without noticeable byproducts. Excessive DIO in such phase transformation process is detrimental, The DIO insulation of $[PbI_6]^{4-}$ cage leads to very low crystallinity of perovskite thin film under a similar time scale, and the poor solubility it provides to perovskite precursors is limited, and sedimentation takes places to reduce thin film crystallinity.

We then extract the crystallization dynamic parameters by conducting the *in situ* GIWAXS experiments at different temperature (60 ℃, and 100 ℃). **Fig 3a, b** show representative 1D GIWAXS profiles for DIO0 and DIO5 samples processed at 60 ℃, and its corresponding peak intensity evolution profiles were shown in **Fig. S6**. It can be noted that the crystallization kinetics for these cases are similar, that is, a direct

phase transition from the intermediate phase to the perovskite phase, which occurred at 8 s for DIO0 case and 48 s for DIO5 case. The elevated substrate temperature eliminates the byproduct formation and increases the excessive DIO vaporization. The delayed phase transition for DIO case originates from the stronger interaction between precursor solution and DIO, and its high-boiling point, which increase the energetic barrier for the perovskite phase formation. Furthermore, a prolonged heating at 60 °C results in the decomposition of perovskite and appearance of PbI_2, as evidenced by the decreased peak intensity of perovskite phase (q=1.0 Å^{-1}) and increased peak intensity of PbI_2 (q=0.9 Å^{-1}), indicating the thermal instability of perovskite without DIO insulation (**Fig. S7a, b**). In contrast, no obviously undesirable peaks appear in the perovskite films with DIO (**Fig. S7c-f**), suggesting that DIO additive can interact with perovskite crystallites, most probably by protecting the crystal surface and boundaries to effectively suppress the high temperature decomposition. Elevating the substrate temperature to 100 °C (**Fig. S8**) leaves very short time window to capture the intermediate phase formation process, especially for DIO0 film. The crystal sizes of different samples are shown in **Fig. S8c, d**, which were determined from the Scherrer equation.[34] It can be observed that DIO additive yields a crystal size of 18.5 nm, which is a bit larger than that of control samples (~17.2 nm).

By circular integrating the scattering peak at q=1.0 Å^{-1} (perovskite phase), we can obtain the peak intensity versus different time, and defined as $I(t)$. Given that the perovskite peak does not exist in the precursor, thus we set this state as $I(0)=0$. At the time point of the complete of perovskite crystallization, the corresponding peak intensity is set as $I(t_{end})$. Combining the above two conditions, the degree of perovskite crystallization $X(t)$ can be determined by the following equation:[35]

$$X(t) = \frac{I(t)}{I(t_{end})} \qquad (1)$$

According to the equation, the $X(t)$ for all three isothermal samples were plotted in **Fig. 3c,d**. Further analysis of $X(t)$ enables the determination of activation energy *Ea* for nucleation and growth, which can be extracted from the following formula:[35]

$$\ln\left(t_{x_2} - t_{x_1}\right) = \frac{Ea}{RT} - \ln K_0 + \ln\left(\beta_{x_2} - \beta_{x_1}\right) \qquad (2)$$

Here, t_{x1} and t_{x2} are the time points at which the transformed fraction is near to 0 and 0.9, respectively. The corresponding time is used to construct the profiles of $\ln\left(t_{x2} - t_{x1}\right)$ versus $1/RT$. As shown in **Fig. 3e, f**, an activation energy of 56.60 KJ mol^{-1} is recorded for DIO0 case and 62.42 KJ mol^{-1} for DIO5 case. The increased activation energy E_a slows down the perovskite crystallization and leaves a long crystallization time window. Even though thin film crystallization can be of heterogeneous nature, prolonged crystallization time in a homogeneous media provides an improved environment for perovskite to form better quality crystals. By analysis the perovskite peak series (**Fig. S9**), a slow FWHM broadening is seen in DIO processed thin films, confirming the success in crystal quality control. It is also seen that by adding DIO, the time and temperature handles can be correlated, providing multivariable thin film morphology control parameters to suit varied morphology optimization needs, which should thus be propagandized.

Furthermore, we investigate the physical properties of perovskite films (e. g. morphology, crystallization, trap density as well as non-radiative recombination) under different processing conditions and to fabricate solar cell devices to evaluate photovoltaic performances. **Fig. 4a-b** show the top-view scanning electron microscopy (SEM) images of control and DIO0.25 spin casted perovskite films. The DIO0.25 based film exhibit an enlarged grain size compared to that of control sample, which is in expectation from the previous *in situ* characterization and analysis. The slower crystallization implies a higher Gibbs free energy, which decreases the number of nuclei and enables the growth of larger grains.[36] In addition, the additive processing prolongs the crystallization time, thus improving the crystallinity of perovskite films, as evidenced by the x-ray diffraction (XRD) spectra (**Fig. S10**). The photoluminescence (PL) and time-resolved photoluminescence (TRPL) spectra of bare and PCBM capped perovskite films are performed to assess the capability of carrier recombination and extraction (**Fig. 4c, Fig. S11, and Table S1**). As shown in **Fig. S11a**, the PL intensity of DIO0.25 films is much higher than that of control samples,

implying an effective suppression of non-radiative recombination. Correspondingly, the carrier lifetime of bare perovskite film is increased from 7.94 ns to 13.54 ns for DIO0.25 case, further confirming the DIO additive-induced defect passivation. Thus trace amount of DIO can be left on perovskite surface and interfaces, performing dual functions other than a phase regulation regent. When PCBM layer is added, drastic PL quenching and short carrier lifetime are observed in DIO0.25 film, indicating an effective charge extraction across the interface. The carrier diffusion length (L_D) is determined by the following equation:[37-39]

$$L_D \approx \frac{2d}{\pi} \sqrt{2(\frac{\tau}{\tau_{quench}} - 1)} \qquad (3)$$

Where d is the thickness of perovskite film, τ is the carrier lifetime, and τ_{quench} is quenched lifetime. The calculated diffusion lengths for control and DIO0.25 films are 137 and 528 nm, respectively (**Table S2**). The longer diffusion length for DIO0.25 film is linked to the increased grain sizes and reduced defects, thus creating better pathways for long distance charge transport, resulting in remarkable performance for DIO0.25-based devices.

Dark *J-V* curves and space charge limited current (SCLC) measurements were combined together as complementary techniques to analyze the recombination as well as the trap state density. As shown in **Fig. 4d**, the significantly reduced reverse dark current suggests that DIO additive can effectively minimize the leakage current. Moreover, DIO additive can improve the carrier injection and transport in perovskite films, as indicated by the improved forward current at high voltage. **Fig. 4e** shows the voltage-dependent ideality factor n, which was derived from the dark *J-V* curves by utilizing the following equation.[40-43]

$$n=(\frac{kT}{q}\frac{dln\,J_d}{dV})^{-1} \qquad (4)$$

Where k is the Boltzmann constant, T is the temperature, and J_d is the dark current. It can be noted that the ideality factor vs voltage curves for control and DIO-based devices exhibit a similar trend. The actual ideality factor can be determined from the plateau in the n-*V* curves, that is, 1.96 for control device and 1.42 for DIO-based

device. The significantly reduced ideality factor suggests an efficient suppression of Shockley-Read-Hall (SRH) recombination in the DIO0.25 processed samples.[44] At the low voltage region where the shunt resistance dominates, the ideality factor is larger than 2. With bias, the ideality factor decreases at a relatively high rate, which could be attribute to the high shunt resistance in DIO0.25 based devices. In the high voltage range, the ideality factor is dominated by the series resistance. The larger the increasing rate of ideality factor n is, the larger the series resistance is. These results suggest that DIO additive can increase the shunt resistance and reduce the series resistance to achieve a high FF.

The space charge limited current (SCLC) measurements were conducted to analyze the trap density based on the electron-only devices with a structure of ITO/SnO$_2$ (40 nm)/MAPbI$_3$ (~340 nm)/PCBM (80 nm)/BCP (~8 nm)/Ag (100 nm) (**Fig. 4f**). The trap density can be determined by the trap-filled limit voltage using the following equation:[45-47]

$$N_t = \frac{2V_{TFL}\,\varepsilon_r\,\varepsilon_0}{qL^2}$$

(5)

Where V_{TFL} denotes the onset voltage of the trap-filled limited region, ε_0 is the vacuum permittivity, ε_r is the relative dielectric constant, and L is the thickness of the film. The calculated trap density for control and DIO-based perovskite film is 2.16×10^{16} cm^{-3} and 1.21×10^{16} cm^{-3}, respectively. The reduced trap density in DIO0.25 processed film is attributed to the enlarged grain size and improved crystallization of perovskite film.

Furthermore, to correlate the processing conditions of perovskite films with the device performance, we fabricated the inverted perovskite solar cells with a device structure of ITO/PTAA/MAPbI$_3$/PCBM/BCP/Ag (**Fig. S12**). **T**he photocurrent density vs voltage (*J-V*) curves and corresponding photovoltaic parameters of perovskite solar cells with different amount of DIO additives are shown in **Fig. S13** and **Table S3**. It can be seen that DIO0.25 results in a highest device efficiency of 20.39%, well exceeding the control device (18.22%). In addition, DIO additive can

also eliminate the *J-V* hysteresis (**Fig. 5a**). To further confirm the accuracy of measurement, external quantum efficiency (EQE) measurements were conducted. The integrated current density from (EQE) curve is consistent with short current density (J_{SC}) from *J-V* curve with a deviation of 1.2% (**Fig. S14**). Furthermore, the steady-state photocurrent and PCE output were measured at a maximum power point for 600 s in **Fig. 5b**, which shows stabilized PCE of 18.13% and 20.20% for control device and DIO-based device, respectively. To evaluate the reproducibility of device performance, we fabricated more than 30 cells for each condition. As shown in **Fig. 5c**, DIO0.25-based devices exhibit a higher average PCE of 19.32% than that of control devices (17.64%). The PCE histograms confirm the reproducibility and reliability of our device performance.

The moisture and thermal stability of the devices are evaluated and results are shown in **Fig. 5d**. The upper figure in **Fig. 5d** shows the humidity stability operated under ambient atmosphere (55%-65% humidity). The control device degrades to ~50% of its initial PCE after 600 h tracking. In contrast, the DIO0.25 based device retains ~89%, indicating significantly improved tolerance to humidity. Also, the DIO0.25 based device exhibits improved thermal stability. It can be noted that the DIO-based device degrades to ~77% of its initial PCE after 200 h continuous heat treatment at 85 ºC, which is higher than that of control device (~62%). These results provide solid evidences to confirm the effectiveness of DIO additive processing in improving device efficiency and stability. Such success lies in the manageable control of the perovskite crystallization kinetics by tuning the intermediate solvated phases, and the capability of DIO in passivating perovskite thin film defects to enhance its semiconducting properties and photovoltaic performances.

Conclusion

In summary, we achieved a significant advance in understanding the key role of additive in perovskite crystallization and film formation process, and constructed a correlation between crystallization behavior and device performance. The *in situ*

GIWAXS data show that a proper amount of DIO additive leads to the formation of multi-stage intermediate phase process. The strong coordination between Pb^{2+} and DIO molecules increases the activation energy for nucleation and crystallization of perovskites, making the perovskite formation process easy to control. While excess DIO additive changes the crystallization process largely, with a larger time window for intermediate phase formation and perovskite formation in DIO-rich environment making the crystallization uncontrollable. By optimizing the DIO amount, a desired perovskite films with low defect density, reduced non-radiative recombination, as well as prolonged carrier diffusion length are achieved. These good properties afford a champion efficiency of 20.39%, higher than that of control device (18.22%). In addition, the moisture stability and thermal stability of the device are also enhanced, with 89% PCEs remained after stored in ambient air (55%~60% humidity) for 600 h and 77% remained under the continuous heating at 85 °C for 200 h.

Experimental section

Materials and solution preparation

The hole transport layer poly(bis(4-phenyl)(2,4,6-trimethylphenyl)amine) (PTAA, Xi'an Polymer Light Technology Corp) were prepared by dissolving 2 mg PTAA in 1 ml chlorobenzene (CB, 99.8%, Acros) solvent. The perovskite precursor solution was prepared by dissolving lead iodide (PbI_2, 98%, TCI) and methylammonium iodide (MAI, 99.998%, Deysol) with a molar ratio of 1.08 into the mixed n,n-dimethylformamide (DMF, 99.8%, Acros) and dimethylsulfoxide (DMSO, 99.8%, Acros) (9:1 vol ratio). DIO was purchased from Sigma Aldrich. PCBM (99.5%, Nano-C) with a concentration of 20 mg/mL was dissolved in CB. BCP with a concentration of 0.5 mg/ml was dissolved into the isopropyl alcohol (IPA).

Device fabrication

Patterned ITO glass substrates (sheet resistance $\leq 10 \ \Omega \ cm^{-2}$) were cleaned consecutively in ultrasonic bath with acetone, detergent, deionized water and IPA, and followed by drying at 70 °C for overnight. After 15 min UV-Ozone treatment, the

PTAA solution was spin coated onto the substrates at 5000 rpm for 30 s and annealed at 150 ℃ for 10 min. To improve the wetting property of substrates, the PTAA film was pre-wetted by spinning 70 µl DMF at 4000 rpm for 10 s. Subsequently, the perovskite precursor solution was spin coated at 4000 rpm for 30 s, and then the anti-solvent CB was dropped onto the films at 8nd s, followed by a thermal annealing treatment at 100 ℃ for 10 min. After the film cooling down to room temperature, PCBM solution was spin coated at 1000 rpm for 60 s to form an 80 nm electron transporting layer. Then, the BCP solution was spin coated at 6000 rpm for 30 s. Finally, 100 nm Al electrodes are thermal evaporated onto the substrates to complete the device fabrication process.

Characterization

The SEM images were measured using Zeiss Ultra Plus Field Emission Scanning Electron Microscope (FE-SEM). The steady-state photoluminescence (PL) spectra were recorded with a spectrophotometer (Jobin Yvon LabRAM HR 800UV), with an excitation wavelength of 325 nm. Time-resolved photoluminescence (TRPL) spectra were checked by Time-Resolved Fluorescence Spectrafluorometer, with the excitation wavelength of 480 nm. The photovoltaic device performance was measured by a Keithley 2400 source meter together with a solar simulator (XES-40S2-CE, SAN-EI Electric Co. Ltd.) equipped with AM 1.5 G filter. The light intensity was calibrated to 100 mW cm^{-2} with a standard monocrystalline silicon solar cell (AK-2000, KONICA MINOLTA, INC, Japan). The photocurrent density-voltage (*J-V*) curves were measured in glovebox from both forward (-0.2 to 1.2 V) and reverse (1.2 to -0.2 V) directions. To calibrate the short current J_{sc}, the EQE of solar cells were measured by device with a lock-in amplifier coupled with a monochromator. The steady-state output of PCE and short current were recorded under constant bias at the maximum power point. For the humidity and thermal stability study, non-encapsulated devices were measured in ambient with a relative humidity of 55%~65% and in nitrogen atmosphere at 85 ℃.

***In situ* GIWAXS characterization**

Before experiment, the mini slot die instrument was installed in a helium box. Then a surveillance camera was used to monitor the solvent flow from the slot die head. Before the coating started, the substrate is pre-aligned and a 0.5° incident angle is used in GIWAXS experiment. As soon as the solution went out, the coating process started immediately. At the same time, the structural information was recorded with typical exposure time of 4.5 s for NDIO case and 5 s for DIO processed cases at room temperature. When the substrate temperature was elevated to 60 ℃ and 100 ℃, the exposure time for each frame was decreased to 0.1 s.

Author contributions

F. L. and J. S. conceived the idea and designed the experiment. J. S. and Q. Z. fabricated the perovskite solar cells and checked the device performance and stability. J. S. and S. X. made a series of film characterizations, including SEM, PL, TRPL, XRD, dark J-V and SCLC. J. S., Q. H. and F. L. prepared the static and in situ GIWAXS experiment and made the following data analysis. J. S. wrote the original manuscript. F. L., and Z. Y. provided constructive suggestions and made revision for the manuscript. All the authors discussed the results and contributed to the manuscript.

Conflicts of interest

There are no conflicts to declare.

Acknowledgements

ReferenceX1   A. Kojima, K. Teshima, Y. Shirai and T. Miyasaka, *J. Am. Chem. Soc.*, 2009, **131**, 6050-6051.

2   National Renewable Energy Laboratory, Best research-cell efficiencies chart (2019); https://www.nrel.gov/pv/cell-efficiency.html.

3   M. Kim, G.-H. Kim, T. K. Lee, I. W. Choi, H. W. Choi, Y. Jo, Y. J. Yoon, J. W. Kim, J. Lee, D. Huh, H. Lee, S. K. Kwak, J. Y. Kim and D. S. Kim, *Joule*, 2019, **3**, 2179-2192.

4   M. M. Tavakoli, M. Saliba, P. Yadav, P. Holzhey, A. Hagfeldt, S. M. Zakeeruddin and M. Grätzel, *Adv. Energy Mater.*, 2019, **9**, 1802646.

5   D. Luo, W. Yang, Z. Wang, A. Sadhanala, Q. Hu, R. Su, R. Shivanna, G. F. Trindade, J. F. Watts, Z. Xu, Y. Tu, Y. Zhang, X. Yang, W. Zhang, R. H. Friend, Q. Gong, H. J. Snaith and R. Zhu. *Science*, 2018, **360**, 1442-1446.

6   D. P. McMeekin, G. Sadoughi, W. Rehman, G. E. Eperon, M. Saliba, M. T. Hörantner, A. Haghighirad, N. Sakai, L. Korte, B. Rech, M. B. Johnston, L. M. Herz and H. J. Snaith. *Science*, 2016, **351**, 151-155.

7   M. Saliba, T. Matsui, J. Y. Seo, K. Domanski, J. P. Correa-Baena, M. K. Nazeeruddin, S. M. Zakeeruddin, W. Tress, A. Abate, A. Hagfeldt and M.

Gratzel, *Energy Environ. Sci.*, 2016, **9**, 1989-1997.

8   M. Saliba, T. Matsui, K. Domanski, J-Y. Seo, A. Ummadisingu, S. M. Zakeeruddin, J-P. Correa-Baena, W. R. Tress, A. Abate, A. Hagfeldt and M. Grätzel. *Science*, 2016, **355**, 206-209.

9   J-P. Correa-Baena, Y. Luo, T. M. Brenner, J. Snaider, S. Sun, X. Y. Li, M. A. Jensen, N. T. P. Hartono, L. Nienhaus, S. Wieghold, J. R. Poindexter, S. Wang, Y. S. Meng, T. Wang, B. Lai, M. V. Holt, Z. H. Cai, M. G. Bawendi, L. B. Huang, T. Buonassisi and D. P. Fenning. *Science*, 2019, **363**, 627-631.

10   M. Abdi-Jalebi, Z. Andaji-Garmaroudi, S. Cacovich, C. Stavrakas, B. Philippe, J. M. Richter, M. Alsari, E. P. Booker, E. M. Hutter, A. J. Pearson, S. Lilliu, T. J. Savenije, H. Rensmo, G. Divitini, C. Ducati, R. H. Friend, and S. D. Stranks, *Nature*, 2018, **555**, 497.

11   N. Li, S. Tao, Y. Chen, X. Niu, C. K. Onwudinanti, C. Hu, Z. Qiu, Z. Xu, G. Zheng, L. Wang, Y. Zhang, L. Li, H. Liu, Y. Lun, J. Hong, X. Wang, Y. Liu, H. Xie, Y. Gao, Y. Bai, S. Yang, G. Brocks, Q. Chen, and H. Zhou, *Nat. Energy*, 2019, **4**, 408-415.

12   L. J. Zuo, H. X. Guo, D. W. deQuilettes, S. Jariwala, N. D. Marco, S. Q. Dong, R. DeBlock, D. S. Ginger, B. Dunn, M. K. Wang and Y. Yang, *Sci. Adv.*, 2017, **3**, 1700106-1700116.

13   B. Chaudhary, A. Kulkarni, A. K. Jena, M. Ikegami, Y. Udagawa, H. Kunugita, K. Ema and T. Miyasaka, *ChemSusChem*, 2017, **10**, 2473-2479.

14   D. Bi, C. Yi, J. Luo, J.-D. Décoppet, F. Zhang, Shaik M. Zakeeruddin, X. Li, A. Hagfeldt and M. Grätzel, *Nat. Energy*, 2016, **1**, 16142.

15   Y. Zhao, J. Wei, H. Li, Y. Yan, W. Zhou, D. Yu and Q. Zhao, *Nat. Commun.*, 2016, **7**, 10228.

16   N. K. Noel, A. Abate, S. D. Stranks, E. Parrott, V. Burlakov, A. Goriely and H. J. Snaith, *ACS Nano*, 2014, **10**, 9815-9821.

17   Q. Z. Zhang, S. B. Xiong, J. Ali, K. Qian, Y. Li, W. Feng, H. L. Hu, J. N. Song and F. Liu, *J. Mater. Chem. C*, 2020, **8**, 5467.

18   J. Xu, A. Buin, A. H. Ip, W. Li, O. Voznyy, R. Comin, M. Yuan, S. Jeon, Z. Ning, J. J. McDowell, P. Kanjanaboos, J. P. Sun, X. Lan, L. N. Quan, D. H. Kim, I. G. Hill, P. Maksymovych and E. H. Sargent, *Nat. Commun.*, 2015, **6**, 7081.

19   L. Han, S. Cong, H. Yang, Y. Lou, H. Wang, J. Huang, J. Zhu, Y. Wu, Q. Chen, B. Zhang, L. Zhang and G. Zou, *Sol. RRL*, 2018, **54**, 1800054.

20   M. Saliba, S. Orlandi, T. Matsui, S. Aghazada, M. Cavazzini, J.-P. Correa-Baena, P. Gao, R. Scopelliti, E. Mosconi, K.-H. Dahmen, F. De Angelis, A. Abate, A. Hagfeldt, G. Pozzi, M. Graetzel and M. K. Nazeeruddin, *Nat. Energy*, 2016, **1**, 15017.

21   W. Y. Nie, H. Tsai, R. Asadpour, J.-C. Blancon, A. J. Neukirch, G. Gupta, J. J. Crochet, M. Chhowalla, S. Tretiak, M. A. Alam, H-L Wang and A. D. Mohite. *Science*, 2015, **347**, 522-525.

22   J. H. Kim, S. T. Williams, N. Cho, C.-C. Chueh and A. K. Y. Jen, *Adv. Energy Mater.,* 2015, **5**, 1401229.

23   P. W. Liang, C. Y. Liao, C. C. Chueh, F. Zuo, S. T. Williams, X. K. Xin, J. Lin and A. K. Jen, *Adv. Mater.*, 2014, **26**, 3748.

24   C.-C. Chueh, C.-Y. Liao, F. Zuo, S. T. Williams, P.-W. Liang and A. K. Y. Jen, *J. Mater. Chem. A*, 2015, **3**, 9058-9062.

25   K. Meng, L. Wu, Z. Liu, X. Wang, Q. Xu, Y. Hu, S. He, X. Li, T. Li and G. Chen, *Adv. Mater.*, 2018, **30**, 1706401.

26   X. Zhang, R. Munir, Z. Xu, Y. Liu, H. Tsai, W. Nie, J. Li, T. Niu, D. M. Smilgies, M. G. Kanatzidis, A. D. Mohite, K. Zhao, A. Amassian and S. F. Liu, Adv Mater, 2018, e1707166.

27   Q. Hu, L. Zhao, J. Wu, K. Gao, D. Luo, Y. Jiang, Z. Zhang, C. Zhu, E. Schaible, A. Hexemer, C. Wang, Y. Liu, W. Zhang, M. Gratzel, F. Liu, T. P. Russell, R. Zhu and Q. Gong, *Nat. Commun.*, 2017, **8**, 15688.

28   J. N. Song, G. Q. Zhou, W. Chen, Q. Z. Zhang, J. Ali, Q. Hu, J. Wang, C. Wang, W. Feng, A. B. Djurisic, H. M. Zhu, Y. M. Zhang, T. P. Russell and F.

Liu, *Adv. Mater.* 2020, 2002784.

29.   M. Alsari, O. Bikondoa, J. Bishop, M. Abdi-Jalebi, L. Y. Ozer, M. Hampton, P. Thompson, M. T. Hörantner, S. Mahesh, C. Greenland, J. E. Macdonald, G. Palmisano, H. J. Snaith, D. G. Lidzey, S. D. Stranks, R. H. Friend and S. Lilliu, *Energy Environ. Sci.*, 2018, **11**, 383-393.

30.   R. Munir, A. D. Sheikh, M. Abdelsamie, H. Hu, L. Yu, K. Zhao, T. Kim, O. E. Tall, R. Li, D. M. Smilgies and A. Amassian, *Adv. Mater.*, 2017, **29**,1604113.

31.   K. Wang, M. C. Tang, H. X. Dang, R. Munir, D. Barrit, M. De Bastiani, E. Aydin, D. M. Smilgies, S. De Wolf and A. Amassian, *Adv. Mater.*, 2019, **31**, 1808357.

32.   M. Qin, K. Tse, T. K. Lau, Y. Li, C. J. Su, G. Yang, J. Chen, J. Zhu, U. S. Jeng, G. Li, H. Chen and X. Lu, *Adv. Mater.*, 2019, **31**, 1901284.

33.   X. Zhang, X. D. Ren, B. Liu, R. Munir, X. J. Zhu, D. Yang, J. B. Li, Y. C. Liu, D. -M. Smilgies, R. P. Li, Z. Yang, T. Q. Niu, X. L. Wang, A. Amassian, K. Zhao and S. Z. Liu, *Energy Environ. Sci.*, 2017, **10**, 2095-2102.

34.   J. Song, M. Zhang, M. Yuan, Y. Qian, Y. Sun and F. Liu, *Small Methods*, 2018, **2**, 1700229.

35.   D. T. Moore, H. Sai, K. W. Tan, D. M. Smilgies, W. Zhang, H. J. Snaith, U. Wiesner and L. A. Estroff, *J. Am. Chem. Soc.*, 2015, **137**, 2350-2358.

36.   N. Ahn, S. M. Kang, J.-W. Lee, M. Choi and N.-G. Park, *J. Mater. Chem. A*, 2015, **3**, 19901-19906.

37.   Lee, E. M. Y. and Tisdale, W. A. *J. Phys. Chem. C*, 2015, **119**, 9005-9015.

38.   G. C. Xing, N. Mathews, S. Y. Sun, S. S. Lim, Y. M. Lam, M. Grätzel, S. Mhaisalkar and T. C. Sum, *Science*, 2013, **342**, 344-347.

39.   S. D. Stranks, G. E. Eperon, G. Grancini, C. Menelaou, M. J. P. Alcocer, T. Leijtens, L. M. Herz, A. Petrozza and H. J. Snaith, *Science*, 2013, **342**, 341-344.

40.   T. Kirchartz, F. Deledalle, P. S. Tuladhar, J. R. Durrant, and J. Nelson, *J. Phys. Chem. Lett.*, 2013, **4**, 2371-2376.

41. O. Almora, K. T. Cho, S. Aghazada, I. Zimmermann, G. J. Matt, C. J. Brabec, M. K. Nazeeruddin and G. Garcia-Belmonte, *Nano Energy*, 2018, **48**, 63-72.

42. P. Calado, D. Burkitt, J. Yao, J. Troughton, T. M. Watson, M. J. Carnie, A. M. Telford, B. C. O'Regan, J. Nelson and P. R. F. Barnes, *Phys. Rev. Appl.*, 2019, **11**, 044005.

43. G. J. Wetzelaer, M. Scheepers, A. M. Sempere, C. Momblona, J. Avila and H. J. Bolink, *Adv. Mater.*, 2015, **27**, 1837.

44. X. Zhao, L. Tao, H. Li, W. Huang, P. Sun, J. Liu, S. Liu, Q. Sun, Z. Cui, L. Sun, Y. Shen, Y. Yang and M. Wang, *Nano Lett.*, 2018, **18**, 2442-2449.

45. J. Qiu, Y. Zheng, Y. Xia, L. Chao, Y. Chen and W. Huang, *Adv. Func. Mater.*, 2018, 1806831.

46. T. Niu, J. Lu, R. Munir, J. Li, D. Barrit, X. Zhang, H. Hu, Z. Yang, A. Amassian, K. Zhao and S. F. Liu, *Adv. Mater.*, 2018, **30**, 1706576.

47. G. Wu, J. Zhou, J. Zhang, R. Meng, B. Wang, B. Xue, X. Leng, D. Zhang, X. Zhang, S. Bi, Q. Zhou, Z. Wei, H. Zhou and Y. Zhang, *Nano Energy*, 2019, **58**, 706-714.

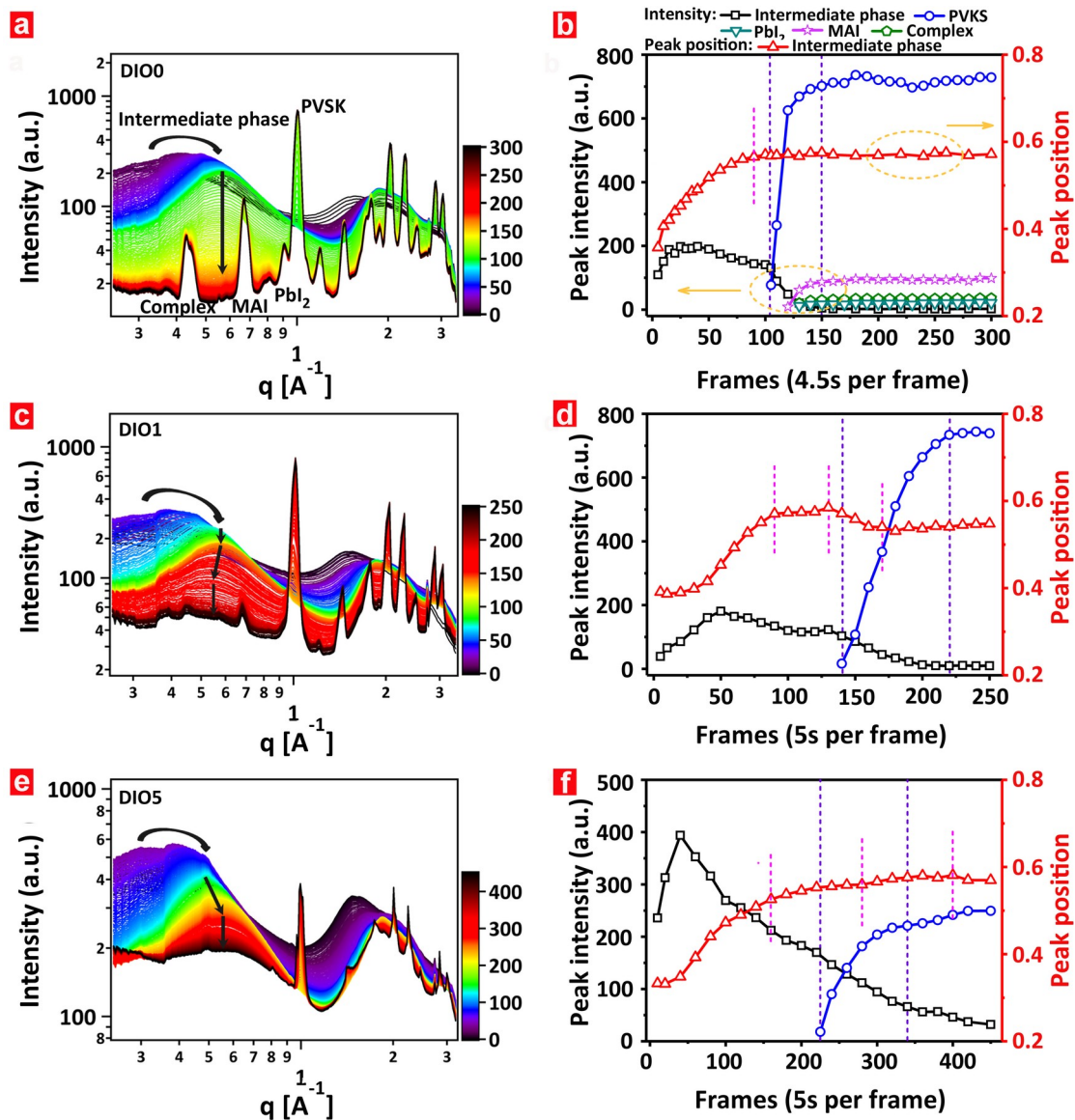**Figures and figure captions**

Fig. 1 *In situ* 1D GIWAXS profiles of perovskite films and its corresponding evolution of characteristic peak intensity along with time: (a, b) DIO0, (c, d) DIO1, and (e, f) DIO5. Here, the perovskite films derived from precursor solution with 0 vol%, 1 vol%, and 5 vol% DIO additive (with respect to main solvent) were abbreviated as DIO0, DIO1, and DIO5, respectively. Complex is the abbreviation of crystalline MAI·PbI$_2$·DMF, and PVSK is abbreviated of perovskite phase. The arrows indicate the shift direction of peak position. Key turning points of intermediate phase peak position were marked by pink dashed lines, and the crystallization stages were marked by the violet dashed lines.
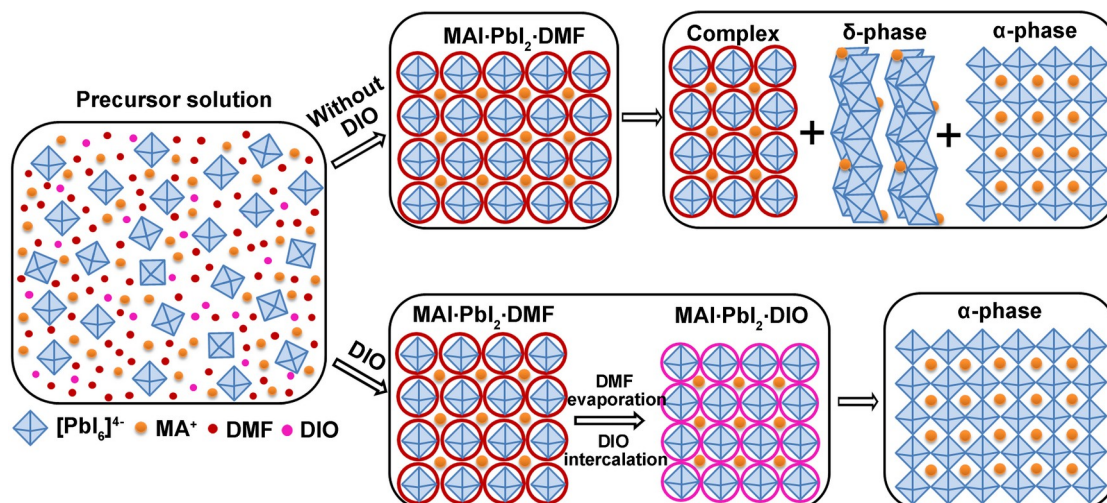
Fig. 2 Schematic diagram illustrating the crystallization kinetics and film formation mechanism of perovskites without and with DIO additive.
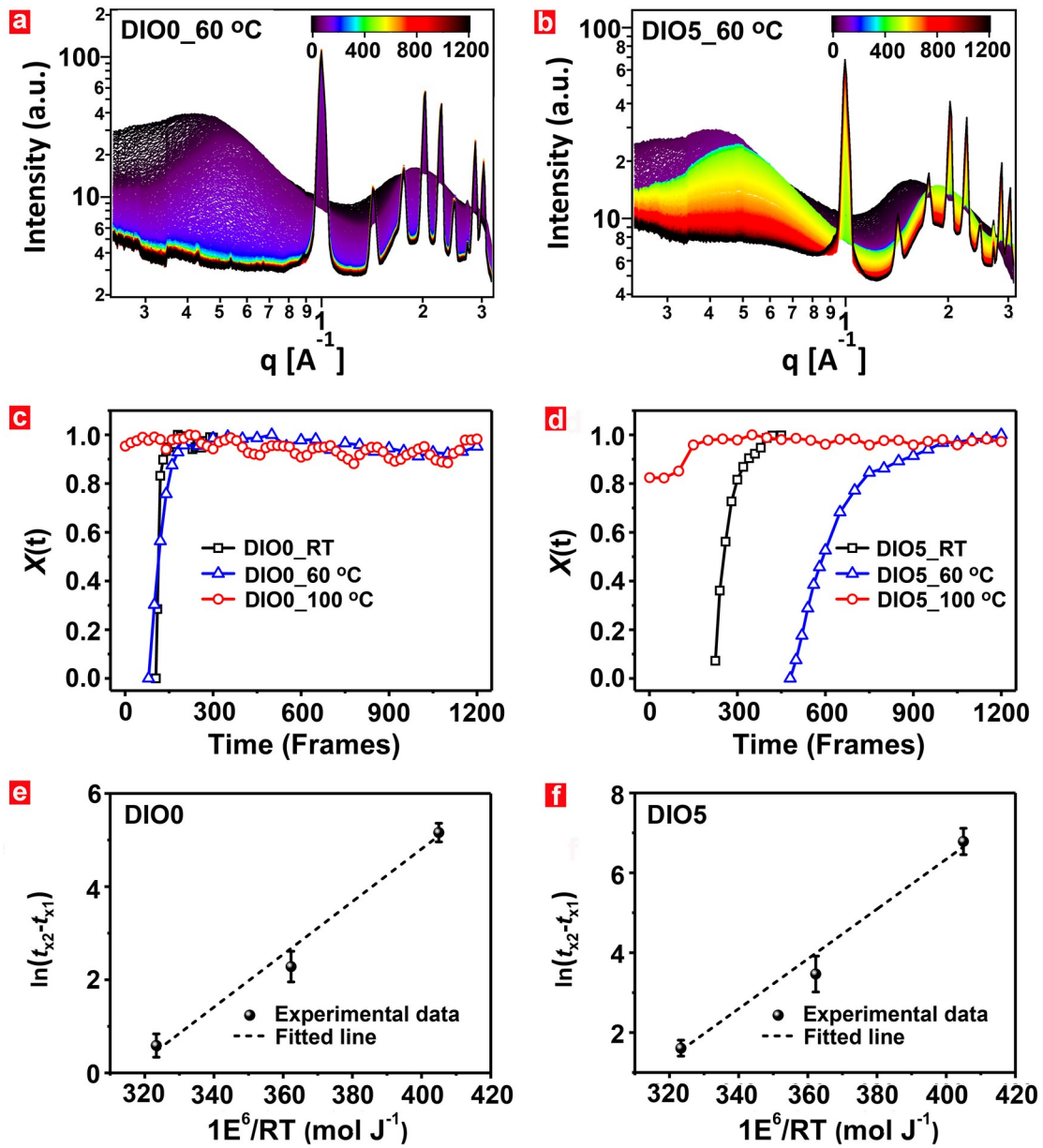
Fig. 3 *In situ* GIWAXS profiles for isothermal perovskite films at 60 °C: (a) DIO0, (b) DIO5. The degree of perovskite formation $X(t)$ plotted as a function of time for isothermal samples at RT, 60 °C, and 100 °C: (c) DIO0, (d) DIO5. The plots of $\ln(t_{x2} - t_{x1})$ versus $1/RT$ profiles for DIO0 (e) and DIO5 (f).
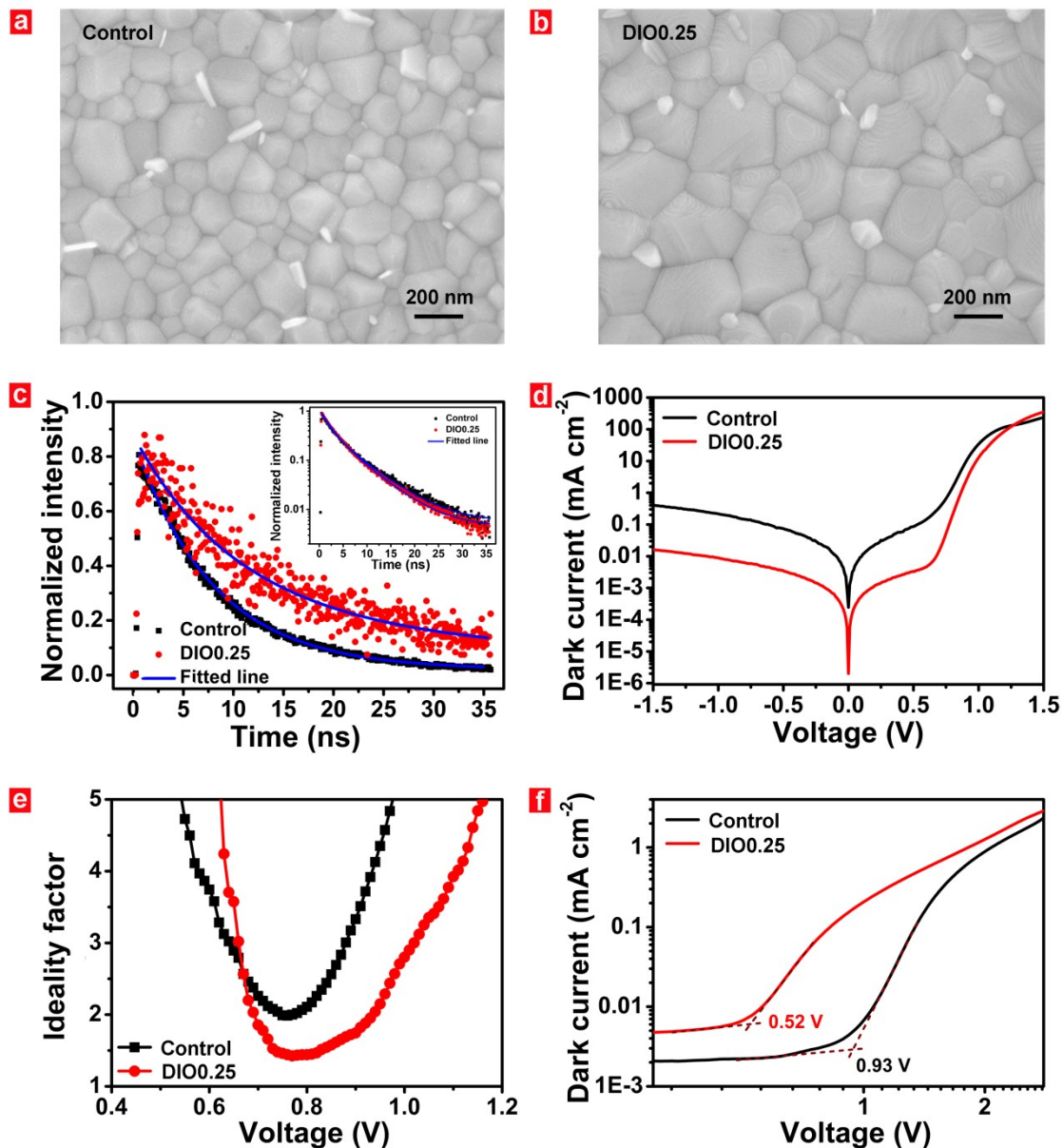
Fig. 4 Top-view scanning electron microscopy (SEM) images of (a) control and (b) DIO0.25 perovskite films. (c) Time-resolved photoluminescence (TRPL) spectra of bare perovskite films. The inset shows the TRPL spectra of PCBM quenched perovskite films. (d) Dark *J-V* curves of control and DIO0.25 based perovskite solar cells. (e) Ideality factor as a function of voltage, which were derived from dark *J-V* curves. (f) *J-V* curves of electron-only devices with a structure of ITO/SnO$_2$ (40 nm)/ MAPbI$_3$ (~340 nm)/PCBM (80 nm)/BCP (~8 nm)/Ag (100 nm).
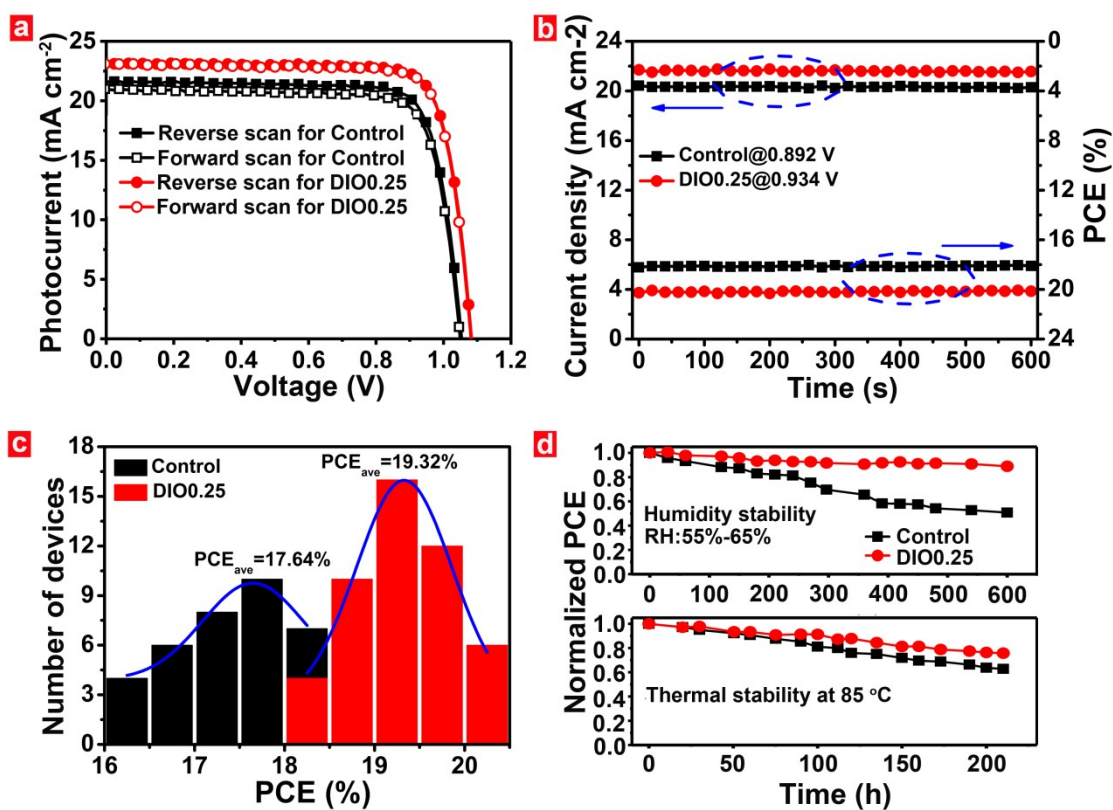
Fig. 5 (a) Photocurrent density versus voltage (*J-V*) curves of perovskite solar cells based on control and DIO0.25 measured in both reverse and forward directions. (b) Steady-state output of current density and PCE at the maximum power point (0.892 V for control device and 0.934 V for DIO0.25-based device). (c) The histograms of PCE for control and DIO0.25 based MAPbI$_3$ perovskite solar cells, which were summarized from above 30 cells. (d) Device moisture and thermal stability study of control and DIO0.25 based non-encapsulated devices in ambient condition with humidity of 55-65% (Upper figure) and nitrogen atmosphere at 85 ℃ (lower figure).